240 (2024) 212933

Contents lists available at ScienceDirect

Geoenergy Science and Engineering

journal homepage: www.sciencedirect.com/journal/geoenergy-science-and-engineering

Surface wetting characterization in pore-scale multiphase flow simulations: A Ketton carbonate case study

Tingting Wang [a], Ying Da Wang [a], Chenhao Sun [b], James E. McClure [c], Peyman Mostaghimi [d], Ryan T. Armstrong [d,*]

[a] School of Minerals and Energy Resources Engineering, University of New South Wales, Sydney, NSW, Australia
[b] State Key Laboratory of Petroleum Resources and Prospecting, China University of Petroleum, Beijing, 102249, PR China
[c] Advanced Research Computing, Virginia Polytechnic Institute and State University, Blacksburg, VA, USA
[d] School of Civil and Environmental Engineering, University of New South Wales, Sydney, NSW, Australia

ARTICLE INFO

Keywords:
Multiphase flow in porous media
Wettability
Pore-scale simulation
Carbonate rock
Phase morphology
Lattice Boltzmann method

ABSTRACT

Direct numerical simulations are commonly applied to X-ray computed microtomography images of porous rocks to measure petrophysical properties, such as relative permeability. To complement and/or expand laboratory data with useful simulations, such simulations need to reflect the true wetting condition of reservoir rock. It is therefore important to investigate approaches for assigning surface wetting conditions in pore-scale multiphase flow simulations. Two-phase Lattice-Boltzmann simulations are conducted on a Ketton carbonate image using different effective wetting models and then compared to pore-scale experimental data on the same rock, which is published elsewhere in (Scanziani et al., 2018). Two different wetting models are established based on the aging of the Ketton sample with crude oil at connate water saturation. *Model 1* provides uniform wetting on all oil treated surfaces. *Model 2* attempts to capture the multiscale nature of carbonate by allowing for spatially varying wetting conditions on oil treated surfaces based on local microporosity. Assessment criteria are based on pore-scale morphological measures, which include oil surface area coverage, oil phase topology, fluid/fluid curvatures, and contact angles. Overall, *Model 1* with an assigned contact angle of greater than +10° above the geometrically measured contact angle from the experimental data provided the best results based on our assessment criteria.

1. Introduction

Wettability is a crucial surface characteristic determining the interactions between rock and fluids in porous media (W. Anderson, 1986). It significantly influences immiscible fluid distribution in reservoirs, affecting effective flow properties like residual oil saturation, relative permeability, and capillary pressure (W. G. Anderson, 1986). Traditional methods, such as the sessile drop technique for contact angle measurement, have provided insights into rock wettability (Kwok and Neumann, 1999). However, these methods are insufficient to accurately represent the wettability distribution within complex porous structures. Therefore, when employing the Lattice Boltzmann Method (LBM), a well-known method for simulating single-phase and multi-phase flows (McClure et al., 2021), accurate determination of wettability conditions becomes a task of utmost importance. Studies such as those conducted by (Jackson et al., 2003), covering multiscale simulations from pore to reservoir scale, illustrate the potential of network models to predict wettability in rocks and its impact on flow. Furthermore, research by (Akai et al., 2019), which compares simulations using constant contact angles with those applying pore-averaged values, underscores the importance of accurately assigning contact angle values to mirror experimental wettability observations. These studies highlight the importance in defining realistic wettability conditions for direct multiphase flow simulations.

In the early stage of wettability research, according to the fact that the minerals that make up reservoir rocks are mostly hydrophilic, the wetting state was assumed to be water wet (Tweheyo et al., 1999). Later, it was considered that after the formation of an oil reservoir, the rock surface will contact oil for geological time, and the active substances in crude oil will adhere to the rock surface, which changes the rock surface from a water-wet to oil-wet or intermediate-wet condition (Tweheyo et al., 1999; Zhou and Morrow, 2000). Assuming that the reservoir rock is homogeneous, the wetting tendency of water or oil would be uniform

* Corresponding author.
E-mail address: ryan.armstrong@unsw.edu.au (R.T. Armstrong).

https://doi.org/10.1016/j.geoen.2024.212933
Received 4 October 2023; Received in revised form 23 April 2024; Accepted 15 May 2024
Available online 15 May 2024

Nomenclature

α	Affinity value
θ	Contact angle, [°]
θ_Y	Intrinsic contact angle, [°]
θ_E	Effective contact angle, [°]
$\varnothing_s$	Solid fraction
W	Wettability index
γ	Interfacial tension, [N/m]
$\overline{SA}$	Surface area normolization
$\overline{\chi}$	Euler normolization normolization

on the rock surface. Uniform wetting could be oil wet, water wet, or intermediate wet. However, due to rock heterogeneity, fluid spatial distributions, and complexity of the crude oil, the actual rock could appear heterogeneous wetting, i.e., with parts of the surface water wet, while other parts are rendered intermediate wet or oil wet (AlRatrout et al., 2018). To what degree the surface heterogeneity needs to be captured in direct pore-scale models is an active area of research (Akai et al., 2019; Arnold et al., 2023; Fan et al., 2020; Foroughi et al., 2020; Murison et al., 2014; Singh et al., 2019).

In laboratory research aimed at understanding these complex wettability phenomena, two prevalent methods are employed to age rock cores to a 'reservoir state'. One is static aging (Zhou and Morrow, 2000), the other is dynamic aging (Sripal and James, 2018). Static aging represents a conventional approach where rock samples are aged in a finite volume of crude oil without fluid flow. Conversely, dynamic aging involves a continuous injection of crude oil throughout the entire duration of the aging process. (Fernø et al., 2010) demonstrated that dynamic aging is more effecive in changing wettability compared to static aging. Additionally, the experiment results of (Fernø et al., 2010) also exhibited that to achieve comparable wettability alterations, static aging requires a longer aging time. After aging, the rock surface will have a wettability alteration and reach a more oil-wet condition than before. For either method the rock core is aged in crude oil at connate water saturation for an extended period. Rock surfaces in contact with oil are rendered oil wet or intermediate wet depending on the period of aging and properties of the crude oil (Morrow, 1990). Of critical consideration is the acid content of the oil whereby more acidic oils are more active at rendering surfaces oil wet (Standnes and Austad, 2000). Now that we have discussed how to change wettability, it is equally important to understand how wettability is characterized.

The wettability of rock is commonly characterized by an experimentally measured contact angle using the sessile drop technique (Kwok and Neumann, 1999). However, this method can only describe the wettability of the pore surface at a specific location and cannot reflect the wettability distribution in the pore space. In addition, contact angle measurements taken on a rock surface are an apparent contact angle at the length scale of the observation and do not necessarily reflect the intrinsic contact angle of a surface. Carbonate rocks, e.g., include micro-porous and macro-porous regions, apparent contact angle measurements are commonly taken at the macro-pore length scale while the underlying microporous structure on the macro-pore surface could influence the measurement (Cassie and Baxter, 1944).

While traditional methods like the sessile drop technique offer insights into rock wettability, the real reservoir conditions are more complicated. (Lin et al., 2016) demonstrated that approximately 80% of the 50 reservoirs they studied were moderately oil wet, i.e., contact angles from 120° to 140°. These moderately oil-wet systems are difficult to identify, and the wettability of core samples from these reservoirs can be easily altered inadvertently. How to truly and completely reconstruct the pore space with realistic wettability assignment is still an important problem to be solved, which is more readily becoming a reality with the development of *in situ* contact angle measurements from X-ray computed microtomography images.

With the mention of *in situ* contact angle measurements as an emerging technique, (Alhammadi et al., 2017) measured *in situ* contact angles between immiscible fluids on segmented X-ray images, they found that for an aged carbonate sample, contact angles were more widely spread than water-wet conditions with values less than and greater than 90°. They measured *in situ* contact angles of three samples (total of 595 million voxels) and reported a mean and standard deviation of 77° ± 21° indicating a weakly water-wet condition with few oil-wet surfaces; 104° ± 26° showing a mixed-wet system with more oil-wet surfaces; and 94° ± 24° illustrating a mixed-wet system with contact angles ranging from water wet to oil wet. Furthermore, (Alhammadi et al., 2017) also observed a wide range of contact angle values in their study on carbonate samples. The three samples were labelled as water-wet (WW), mixed-wet (MW), and oil-wet (OW). The average contact angles for these samples were measured as 76°, 93°, and 103°, respectively. In addition, contact angle measurements were performed on flat calcite surfaces, resulting in average contact angle values of 76°, 130°, and 141°, using the same fluids. Notably, for the mixed-wet (MW) and oil-wet (OW) samples, *in situ* contact angles were generally lower on average compared to those measured on flat surfaces, suggesting that the presence of surface roughness tends to decrease the apparent oil wetness of the rock.

Herein, we investigate various ways to assign surface wettability in a digital rock model that aims to mimic the wettability of an aged-carbonate core. We focus on Ketton carbonate because of the rich amount of experimental and simulation results available in the literature on it (Menke et al., 2015; Rücker et al., 2019; Scanziani et al., 2018), include pore-scale analysis for water-wet and intermediate-wet conditions. Additionally, Ketton provides an ideal sample for studing wettability due to its multiscale structure, i.e., well-resolved macro-pores and clear scale separation of microporosity on the pore surfaces. To study Ketton, we take a targeted assignment of surface wettability, which can be changed from initially water wet to oil wet through the simulated contact of oil with the rock surface. After primary drainage, all rock surfaces in contact with oil are set to be oil wet, and all other surfaces remain water wet to mimic the aging process. Our proposition is that to what degree the oil-wet regions become oil wet depends on the microporosity of the macroporosity pore walls. Micropores retain water, and thus potentially remain water wet (to a degree) since the capillary pressure required to drain the microporosity is restrictively high. This impact on wettability will in turn influence multiphase flow in the macropores, as evident in pore-scale phase morphologies and the resulting relative permeability at the continuum scale. For validation, we compare pore-scale experimental images of fluids in an aged-carbonate core to those simulated under various wetting conditions. The Minkowski Functionals (MFs) are used to compare the fluid phase morphologies and contact angle measurements are used to understand the wetting condition and the influence that microporosity has on the apparent (effective) contact angle. Finally, we found that the uniform wetting models, characterized by a uniform contact angle, can effectively represent the wettability conditions in Ketton carbonate rocks dispite the complexities associated surface heterogeneity and microporosity. Lastly, we report on how our wettability assignment influnces the continuum scale property of relative permeability.

2. Materials and methods

2.1. X-ray computed microtomography data

Two data sets were selected from the Digital Rocks Portal (https://www.digitalrocksportal.org/).

Dataset 1 comprises greyscale and segmented multiphase images, but no experimental images, while Dataset 2 does not contain an original greyscale image but does contain segmented multiphase images of an

aged-carbonate core during an imbibition experiment. Dataset 2 was reported as a mixed-wet sample (Scanziani et al., 2020b) with an average contact angle of 109°. The experimental data shows an initial water saturation of only 0.1% in the macropores; suggesting that the aging procedure was conducted with the core at a nearly fully oil saturated macroporosity with water residing in the microporosity only.

2.2. Wettability assignment

The mixed wetting nature of these cores was mapped onto the surface of the solid voxels by identifying whether solid voxels are in contact with water or oil after a primary drainage simulation. The workflow for contact angle assignment is provided in Fig. 1. We assume that after primary drainage, the phase distributions are static, and over time, the wettability of the surfaces in contact with oil are altered, i.e., dynamic aging of the surface is not considered. The wettability of the domain is therefore mixed-wet, with surfaces in contact with water remaining water wet, and surfaces in contact with oil becoming oil wet. The exact contact angles to be assigned to the water-wet and oil-wet regions are discussed in Section 3.

2.3. Lattice Boltzmann simulations

Two-phase Lattice Boltzmann Method (LBM) simulations were carried out on Datasets 1 and *2*. The details of the implementation are provided by (McClure et al., 2021), and a brief explation is provided below.

In LBM [4], surface wetting affinity towards two fluids is represented by a scalar value α, ranging from -1 to $+1$: -1 is related to oil wet and $+1$ is related to water wet. This automatically recovers the expected contact line and contact angle behaviour at both dynamic and static conditions (McClure et al., 2021). On a flat surface of affinity α, the static contact angle can be defined as

$$\cos\theta = \alpha. \tag{1}$$

This angle can be considered as an effective (or apparent) contact angle at the pore scale. All simulations were conducted at a Capillary number of 1×10^{-5}. The simulations are firstly performed under unsteady state injection conditions that emulate the injection of water into the domain, which is initially saturated with water and oil at the irreducible water saturation. This initial fluid distribution is obtained experimentally from micro-CT images of aged samples as outlined in Section 2.1, and following the assignment of the surface wettability based on this initial experimental fluid distribution and the micro-CT image outlined in Section 2.3, a 100% water saturation inlet coundary conditions is injected into the domain using a pressure difference that results in the aforementioned capillary number until the irreducible oil saturation is reached. The simulation protocol for obtaining the relative permeability of an aged sample involves a steady-state simulation process at varying saturations, mimicking a co-injection steady state laboratory experiment. An accelerated technique is used that involves the coupling of LBM simulations and morphological operations on the fluid clusters (Wang et al., 2020) to rapidly converge the LBM simulation to steady state conditions at successive saturation points with periodic boundary conditions applied in this case to minimise capillary end effects and non-uniform saturation profiles.

2.4. Contact angle models

We consider two methods for assigning effective contact angles to water-wet and oil-wet regions.

Model (1) Uniform Wetting: we assume that the surfaces are smooth, impermeable, and homogenous. Therefore, a single effective contact angle is assigned to the oil-wet regions and likewise for the water-wet regions.

Model (2) Cassie-Baxter Wetting: we assume that the grain surfaces are microporous and retain water which thereby influences the effective contact angle. This is reasonable for carbonate rocks given that the capillary pressure required to penetrate the microporosity during aging is typically not exceeded in experiments nor under geological conditions (McPhee et al., 2015).

We follow the microporosity analysis method presented by (Lin et al., 2016). The CT value of a voxel is proportional to the voxel density, therefore the solid fraction on a per voxel basis is defined as

$$\varnothing_s = \frac{CT_{voxel} - CT_{macropores}}{CT_{grain} - CT_{macropores}}, \tag{2}$$

where $\varnothing_s$ is voxel solid fraction, CT_{voxel} is the CT number of each voxel, $CT_{macropores}$ is the average CT value of macropores, and CT_{grain} is average CT value of the grains.

Based on the assumption for *Model 2*, during aging the fraction of the carbonate rock surface that is exposed to oil depends on the surface microporosity. This means that only a fraction of a given surface voxel is rendered oil wet. The Cassie-Baxter model (Cassie and Baxter, 1944) provides a means to define this condition as

$$\cos\theta_E = \varnothing_s \cos\theta_Y + (1 - \varnothing_s), \tag{3}$$

where $\varnothing_s$ is the carbonate voxels solid fraction in contact with the oil surface, θ_Y is the intrinsic contact angle of a solid carbonate surface, and θ_E is the effective contact angle observed in a pore-scale image.

In *Model 1*, the grain surfaces are assigned a uniform effective contact angle (θ_E) while with *Model 2* an intrinsic contact angle (θ_Y) is predefined and θ_E is determined based on the grain surface microporosity. For either model a user defined contact angle must be chosen. The reported average *in situ* contact angels for the experimental data was 110 ° degrees (Scanziani et al., 2018) while experimental sessile drop data in (Treiber and Owens, 1972) reported contact angles up to 160 ° for carbonate rocks. Indeed, it is well known that the wetting condition depends on the oil used, acid number, and treatment method used to age the core (Jadhunandan and Morrow, 1995), and thus (Treiber and Owens, 1972) only provides a general guide. Lastly, it has also been

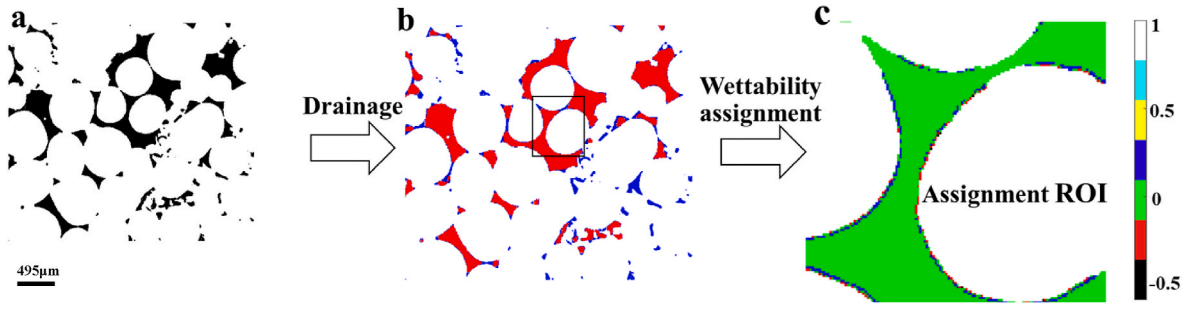

Fig. 1. The workflow for the assignment of contact angles; (a) is the binary image (black = pore, white = grain); (b) is the image after drainage (red = oil, blue = water, white = grain); (c) is the Region-Of-Interest (ROI) image after wettability assignment.

shown that direct *in situ* contact angle measurements can under predict contact angles by ~20 ° at high contact angle values (Sun et al., 2020).

For *Model 1*, we considered a uniform contact angle of $\theta_E = 130°$ for oil-treated surfaces by considering the experimental results from (Scanziani et al., 2018) and assuming an error of 20 °, as reported by (Sun et al., 2020). For *Model 2*, two different approaches could be taken.

1. We considered $\theta_Y = 130°$ for oil-treated regions by taking a representative value of sessile drop data from (Treiber and Owens, 1972).
2. We estimated θ_Y by using Equation (3). Based on Fig. 2, the carbonate rock had an average microporosity of 0.18. Therefore, θ_Y of the oil-treated surfaces would have been approximately 160° based on the measured average microporosity and based on (see Fig. 3a, Fig. 3b).

For all models, macroporosity surface regions that retrained connate water after primary drainage were assigned an effective contact angle of 40°.

The wettability of each model was characterised by a wettability index, where $\varnothing_s$ is the solid voxel fraction of mineral *s*, γ_{so} is the interfacial tension between mineral *s* and oil phase, *o*, and γ_{sw} is the interfacial tension between mineral, *s*, and the water phase, *w*. This equation provides a range from strongly water-wet ($W = 1.0$) to strongly oil-wet ($W = -1.0$),

$$W = \sum (\gamma_{so} - \gamma_{sw}) \Big/ \gamma_{wo} \varnothing_s. \tag{4}$$

The wettability index for each simulation is listed in Table 2.

In Table 1, 'CB' stands for the Cassie-Baxter wetting model, with the following numbers (e.g., 0.65, 0.84, 0.99) representing the oil-wet fraction, indicating the fraction of the pore space that was rendered oil wet. 'CB_Unfixed' indicates here that the partial volume effect (see Section 3.1) is not fixed, while 'CB_Fixed' indicates simulations with a fixed partial volume effect. Additionally, 'Uni' stands for the Uniform wetting model, with subsequent numbers indicating the oil-wet fraction, and 'CA' followed by a number (e.g., 90, 130) specifying the contact angle used. For instance, 'Uni_0.99_1_CA90′ denotes the simulation conducted with Dataset 1 under a contact angle of 90° using *Model 1*. Lastly, EXP represents experimental data.

2.5. Pore-scale morphologies

For a quantitative comparison between simulation and experimental results, we measure the following pore-scale morphological parameters: surface area, Euler characterisitic, curvature, and contact angle. These parameters include the well-known Minkowski functionals, as explained in Appendix A.

Table 1
Summary of X-ray microtomography dataset used in the study.

Dataset No.	Project DOI	Resolution (μm/voxel)	Rock Type	Wettability	Data Source
Dataset 1	10.17612/P7HT11	5	Ketton	Water-wet	Laboratory micro-CT
Dataset 2	10.17612/3S3K-EE20	3.5	Ketton	Mixed-wet	Synchrotron

Table 2
Summary of the conducted simulations. The drainage saturation corresponds to the saturation at which surface wettability was assigned.

Simulation Name	Dataset	Wetting Model	Oil-Wet Fraction	Contact Angle	Wetting Index
CB_0.65_1	1	Cassie-Baxter	0.65	θ_Y = 130°	0.52
CB_0.84_1	1	Cassie-Baxter	0.84	θ_Y = 130°	0.35
CB_0.99_1	1	Cassie-Baxter	0.99	θ_Y = 130°	0.00
CB_Unfixed	1	Cassie-Baxter	0.99	θ_Y = 130°	0.00
CB_Fixed	1	Cassie-Baxter	0.99	θ_Y = 130°	−0.22
Uni_0.99_1_CA90	1	Uniform	0.99	$\theta_E = 90°$	0.00
Uni_0.99_1_CA130	1	Uniform	0.99	θ_E = 130°	−0.64
Uni_0.99_2	2	Uniform	0.99	θ_E = 130°	−0.64
EXP	2	Aged Core	0.99	θ_E = 109°	−0.33

The reported surface area values are determined as

$$\overline{SA} = \frac{M_1\left(\frac{oil}{grain}\right)}{M_1(grain)}, \tag{5}$$

where $M_1(grain)$ is the total surface area of all grain surfaces and $M_1\left(\frac{oil}{grain}\right)$ is only the oil-grain surface area. In this way, we measure surface area coverage following the work of (Garfi et al., 2020).

The reported Euler characteristic values were determined as

$$\overline{\chi} = \frac{\chi(oil)}{\chi(pore\ space)}, \tag{6}$$

where $\chi(oil)$ is the Euler characteristic of the oil phase and $\chi(pore\ space)$ is the Euler characteristic of the pore space. Normalization by the con-

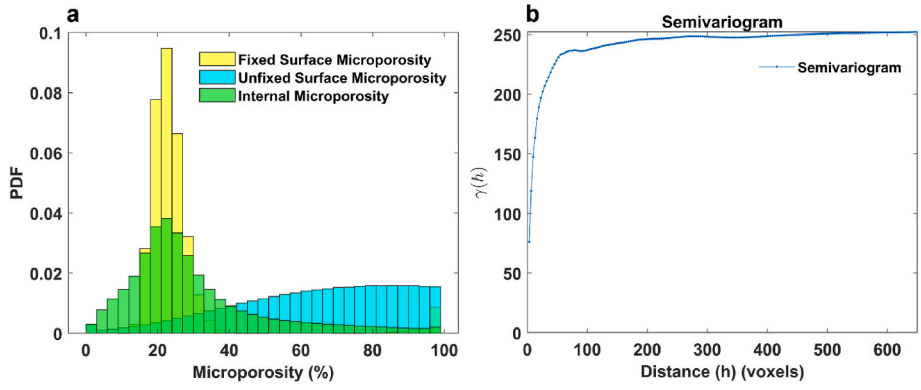

Fig. 2. Micro-porosity analysis. (1) Unfixed Surface Microporosity is distribution of micro-porosity values for voxels that represent the grain surface. (2) Internal Microporosity is the distribution of micro-porosity values that are at least 3 voxels from the surface. (3) Fixed Surface Microporosity is the distribution of the surface microporosity distribution with the same average and spatial statistics as the internal microporosity b. Semi-variogram of the fixed microporosity.

nectivity of the pore space provides insight into how the oil phase fills the pore space.

For curvature, we focus on the fluid/fluid interfacial curvature (μm^{-1}) distributions. We measure the mean curvature distribution and provide the proportions of that distribution include saddle-shaped, convex, and concaved distriubtions. Curvatures were measured using the method provided in (Da Wang et al., 2024).

Contact angles we measured on the segmented images. The direct contact angle measurement method presented by (Da Wang et al., 2024) was used. This method provides the angles throughout the segmented image along the 3-phase contact loops made by the oil/water/solid surfaces. The algorithm first performes connected components isolation of fluid clusters (in this case, the oil phase), meshes and smooths the isolated clusters using merching cubes and Laplacian smoothing, and computes the dot product of the water-oil and oil-solid normal vectors at the contact loop.

3. Results

The results section is organized into three subsections: Microporosity Analysis, Pore-scale Morphologies, and Relative Permeability. First, we will discuss the simulation domain and assignment of microporosity. Simulation results are then compared to experimental results by using various pore-scale metrics. Lastly, we evalute to what degree our proposed wetting models impact the simulated relative permeability.

3.1. Microporosity analysis

For the implementation of *Model 2*, the microporosity of the carbonate grain surfaces needs to be accurately characterised. However, the difficulty with measuring the microporosity of grain surfaces is demonstrated in Fig. 2a. Three distributions of microporosity are presented: (1) Unfixed microporosity values on a grain surface; (2) Internal values at least 3 voxels away from a grain surface, and (3) Fixed microporosity values on a grain surface. Due to the partial volume effect during imaging, the grain surface voxels have CT values preferentially less than those values within the grains (Wildenschild and Sheppard, 2013). This results in high micro-porosity on the grain surface, which in turn results in water-wet conditions when Equation (3) is applied. We therefore decided to run *Model 2* simulations with and without this partial volume effect.

The partial volume effect at the surface voxels of the solid was removed by a stochastic method. The internal microporosity histogram distribution was sampled from at least 3 voxels deep (based on a Elucidean distance map) within the solid/microporous phase, see 'Internal Microporosity' distribution in Fig. 2a. This choice of 3 voxels is made based on visual observation of the length of the blur at an interface, see (Clausnitzer and Hopmans, 1999). The choice of a value greater than 3 should result in the same statistical distribution, while a lower value would begin to include the partial volume voxels. The surface voxels were then replaced by microporosity values sampled from Monte-Carlo simulation of the internal microporosity histogram distribution. The resulting stochastic field was then passed through a Gaussian filter with a correlation length equal to the semi-variogram range of the internal microporosity, see Fig. 2b. The result is a surface microporosity distribution with the same average and similar spatial statistics as the internal microporosity, see Fig. 2a 'Fixed Surface Microporosity'.

3.2. Pore-scale morphologies

In total, eight simulations were conducted, and Region-Of-Interest (ROI) images of these simulations are provided in Fig. 3a. Fig. 3b offers a zoomed-in view of Fig. 3a for a more detailed comparison. The oil phase renderings are ordered from water wet to oil wet. An image pair ($S_o = 0.5$, $S_o = 0.8$) is presented for each simulation. The final image pair (q, r) is the experimental data. Firstly, we observe that oil connectivity improves with increasing oil saturation. Secondly, the oil adheres to the solid surface in both models but much less so for *Model 2* than *Model 1*. Thirdly, the initial oil saturation used to mimic the core aging procedure clearly impacted the simulation results. Lastly, the image pair (3i, 3j) appears to show a more oil-wet condition than image pair (3g, 3h), which demonstrates that the simulation 'CB_Fixed' removed the partial

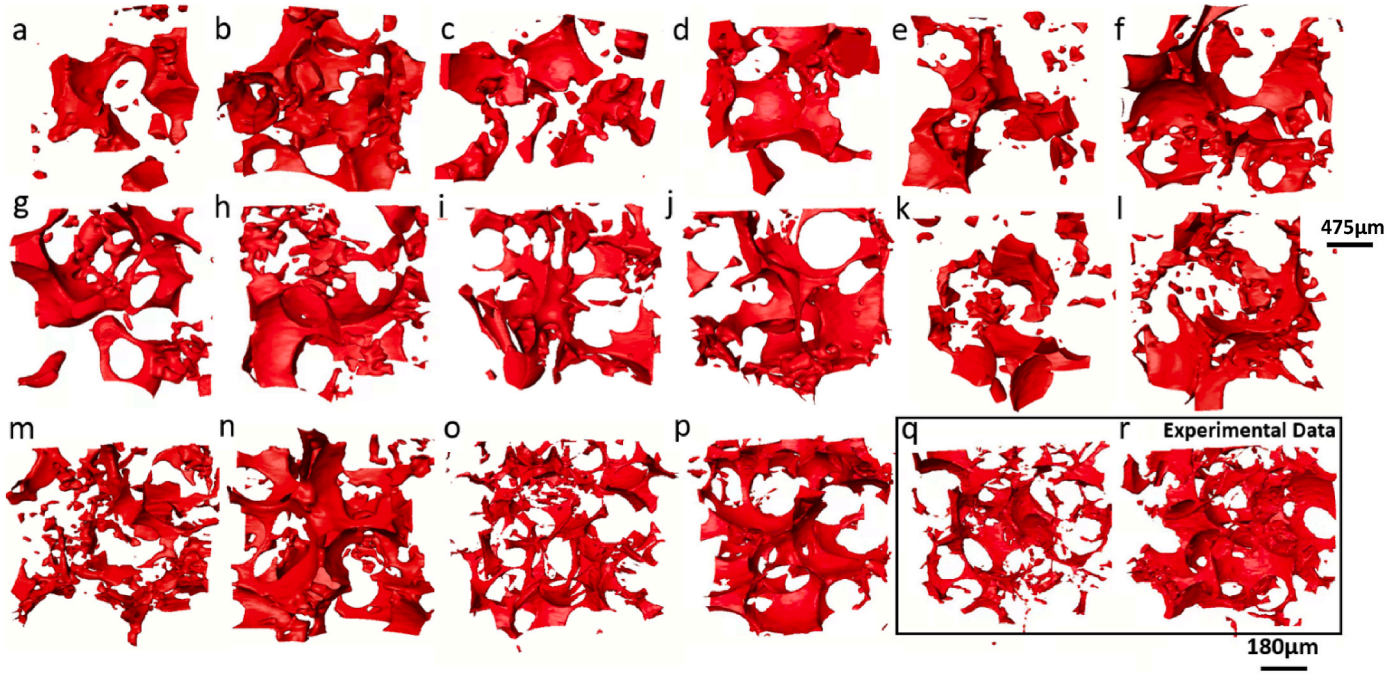

Fig. 3a. Three-dimensional renderings of oil for five simulations and one experiment at oil saturations of 0.5 and 0.8; (a, b) are from simulation CB_0.65_1; (c, d) are from simulation CB_0.84_1; (e, f) are from simulation CB_0.99_1; (g, h) are from simulation CB_Unfixed_1; (i, j) are from simulation CB_Fixed_1; (k, l) are from simulation Uni_0.99_1_CA90; (m, n) are from simulation Uni_0.99_1_CA130; (o, p) are from simulation Uni_0.99_2; and (q, r) are the experimental data. See Table 1 for full details on each simulation case. Overrall, the rendering in (o, p) qualitatively reflect the oil morphologies observed in the experimental data.

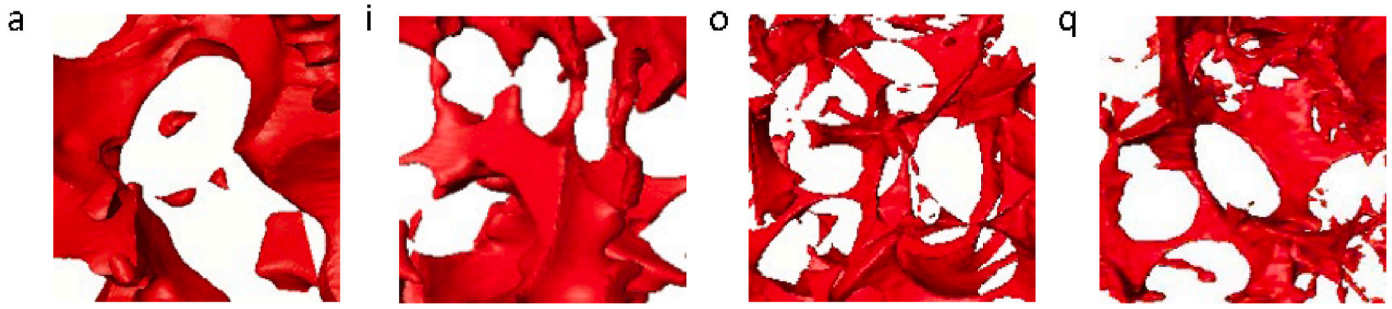

Fig. 3b. Zoomed in three-dimensional renderings of oil for three simulations and one experiment at oil saturations of 0.5; (a) is the zoomed-in view from simulation CB_0.65_1; (i) is the zoomed-in view from CB_Fixed; (o) is the zoomed-in view from Uni_0.99_2; and (q) is the zoomed-in view from experimental data.

volume effect in part and fixed the more water-wet condition created by the Cassie-Baxter model. Overall, the rendering in Fig. 3o and p qualitatively reflect the oil morphologies observed in the experimental data. These renderings correspond to simulation Uni_0.99_2 (see Table 2), which reflects an oil-wet state ($W = -0.64$) with oil coating the grain surfaces.

In Fig. 4, we provide quantitative measures of oil morphology. As oil fills the pore space, $\overline{\chi}$ approaches 1. For oil-wet cases, however, as observed by our simulation results and the experimental data, the oil phase can become more connected than the pore space, i.e., $\overline{\chi} > 1$. This occurs due to the oil forming multiple loops on the grain surfaces under highly oil-wet conditions.

The results of the simulations conducted on the CB_Unfixed and CB_Fixed, as presented in Fig. 4, demonstrate that the partial volume effect can be effectively mitigated by adopting a more appropriate voxel value distribution on the solid surface. Further analysis by comparing the simulations of CB_0.65_1, CB_0.84_1 and CB_0.99_1, indicates that the initial oil saturation had a considerable impact on the results. Specifically, the increase in initial oil saturation resulted in an increase in both $\overline{SA}$ and $\overline{\chi}$ for these simulations. Additionally, the uniform cases and CB_Fixed simulations show an initial increase in $\overline{SA}$, followed by a decrease, as the oil saturation increased. Moreover, the Euler number becomes more negative as the initial oil saturation increased for CB_0.65_1, CB_0.84_1, CB_0.99_1, CB_Unfixed, and Uni_0.99_1_CA90 simulations. However, for the other simulations, the Euler number initially increased and then decreased. These results suggest that the initial oil saturation and the chosen wettability model significantly affects the evolution of phase morphologies.

The results from 'Uni_0.99_2' and 'Uni_0.99_1' provided the best morphological match with the experimental data, as presented in Fig. 4. While the morphological values do not provide an exact match with the experimental data the values are similar, and the overall trends are captured. In particular, the surface area coverages for both simulations are similar to the experimental data and the trend of increased connectivity of the oil phase at intermediate saturations occurs for both simulations. The nonmonotonic behaviour in $\overline{\chi}\,(S_w)$ appears to be a key characteristic for highly oil-wet conditions as observed on both the experimental and simulation data. It should also be noted that an exact match in morphological characteristics would not be expected given that the model domain and boundary conditions are not 1:1 with the experiment.

For the boundary condition, flow outside of the experimentally imaged region is unknown, and thus simulated boundaries were not necessary equivalent to experimental conditions. For the domains, Dataset 1 was the same domain as the experimental data, but the analysis was not performed in the same region as the experimental analysis. This was done to remove any subjective influence that an exact domain-to-domain match could cause, i.e., over-fitting of the model. Instead, the focus should be on the general trends in morphological features. Also, Dataset 2 was a completely different imaged domain of the same rock type. Therefore, the influence of pore morphology could be observed when comparing the 'Uni_0.99_2' and 'Uni_0.99_1' results even though the rock type used was the same for both simulations.

Table 3
Quantitative Error Comparisons for Surface Area and Euler characteristic at oil saturations of 0.5.

Simulation Name	Dataset	Wetting Model	$\overline{SA}$ (%)	$\overline{\chi}$ (%)
CB_Fixed	1	Cassie-Baxter	20.6	75.8
Uni_0.99_1_CA130	1	Uniform	3.6	66.3
Uni_0.99_2	2	Uniform	8.5	29.1

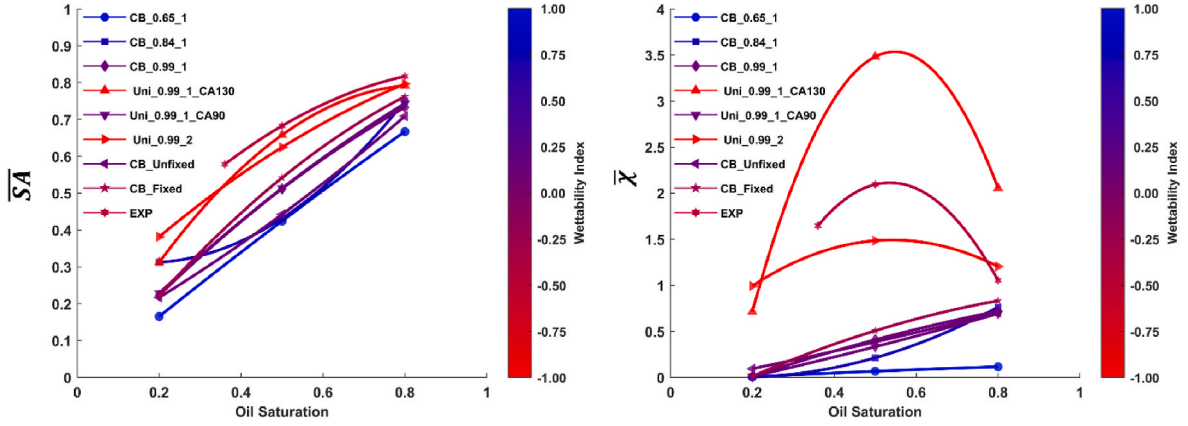

Fig. 4. (a) Surface area normalization (oil-grain surface area/total grain surface area) (b) Euler normalization (Euler of NWP/Euler of pore space) of 8 simulations and experimental data. The reported value at oil saturation of 0.2 is not the residual oil saturation. Overall, the results from 'Uni_0.99_2' and 'Uni_0.99_1' provided the best morphological match with the experimental data.

Quantitative error metrics are presented in Table 3. From $\overline{SA}$, we can see 'Uni_0.99_1_CA130' aligns closely with the experimental data. Additionally, 'Uni_0.99_2' matches the experimental data more accurately when considering $\overline{\chi}$, supporting the visual evidence observed in Fig. 4. Overall, 'Uni_0.99_2' appears to provide the lowest average percent difference when considering both $\overline{SA}$ and $\overline{\chi}$.

In Fig. 5, we compare the fluid/fluid interfacial curvature (μm^{-1}) distributions for Uni_0.99_1, Uni_0.99_2, and CB_Fixed simulations to the experimental data. A significant number of minimal surfaces (saddle shaped surfaces) are identified for all simulations and experimental data. Although the mean curvature of these surfaces is zero, the Gaussian curvature is not. These surfaces exhibit two Gaussian curvatures with equal values but opposite directions, indicating good connectivity between the oil and water phases (Lin et al., 2019; Shojaei et al., 2022). Moreover, the Gaussian curvature is not only indicative of good connectivity but has been interpreted as an indication of mixed-wet conditions (Lin et al., 2019). The findings of (Lin et al., 2019) reported the presence of numerous hyperbolic points on surfaces where the principal curvature is in different directions. These hyperbolic points are indicative of the mixed wetting conditions created during core aging at connate water saturation (core aging details provided in (Imperial College London et al., 2019)). However, mostly uniform affinity values were assigned for the simulations reported herein, which contradicts the concept of mixed wetting. Both 'Uni_0.99_1' and 'Uni_0.99_2' are characterised by a single intermediate-wet affinity value ($\alpha = -0.64$) for 99.9% of the macropore surface voxels.

Fig. 6 presents the distribution of contact angles for the 'Uni_0.99_1', 'Uni_0.99_2', 'CB_Fixed' models, and experimental data using the direct contact angle measurement method presented by (Da Wang et al., 2024). The results indicate that the contact angle distributions for 'Uni_0.99_1', 'Uni_0.99_2' and 'CB_Fixed' are all comparable to the experimental data. The 'CB_Fixed' model shows a reasonable average contact angle value after alleviating the partial volume artifact effects. This is attributed to the accurate representation of surface wettability by the CB_Fixed model. In addition, the average contact angle values for 'Uni_0.99_1', 'Uni_0.99_2', 'CB_Fixed' models are 134°, 133.8°, and 115.8°, respectively. The contact angle derived from the experimental data by (Scanziani et al., 2020a) was 109°, measured using the method of (AlRatrout et al., 2017). While the method reported by (Da Wang et al., 2024) resulted in a measurement of 122°. This discrepancy is primarily due to the different measurement methodologies employed. Yet the measured average values from these simulations were greater than that measured for the experimental data and better aligned with the affinity value assigned in these models, i.e., corresponded to a mostly uniform contact angle of 130°. This indicates that an assigned contact angle of greater than +10° above the geometrically measured contact angle from experimental data should be used.

3.3. Relative permeability

Fig. 7 displays the relative permeability curves on a logarithmic scale for two representative models. *Model 1* is illustrated by 'Uni_0.99_2', while *Model 2* is represented by 'CB_Fixed'. The curves demonstrate a notable difference at their endpoints. With 'CB_Fixed', the oil phase ceases to flow at a water saturation of 0.75, whereas with 'Uni_0.99_2', oil phase stops flowing at a higher water saturation of 0.86. This suggests a lower residual oil saturation of approximately 0.14 in 'Uni_0.99_2', indicative of a more intermediate wetting condition and an enhanced

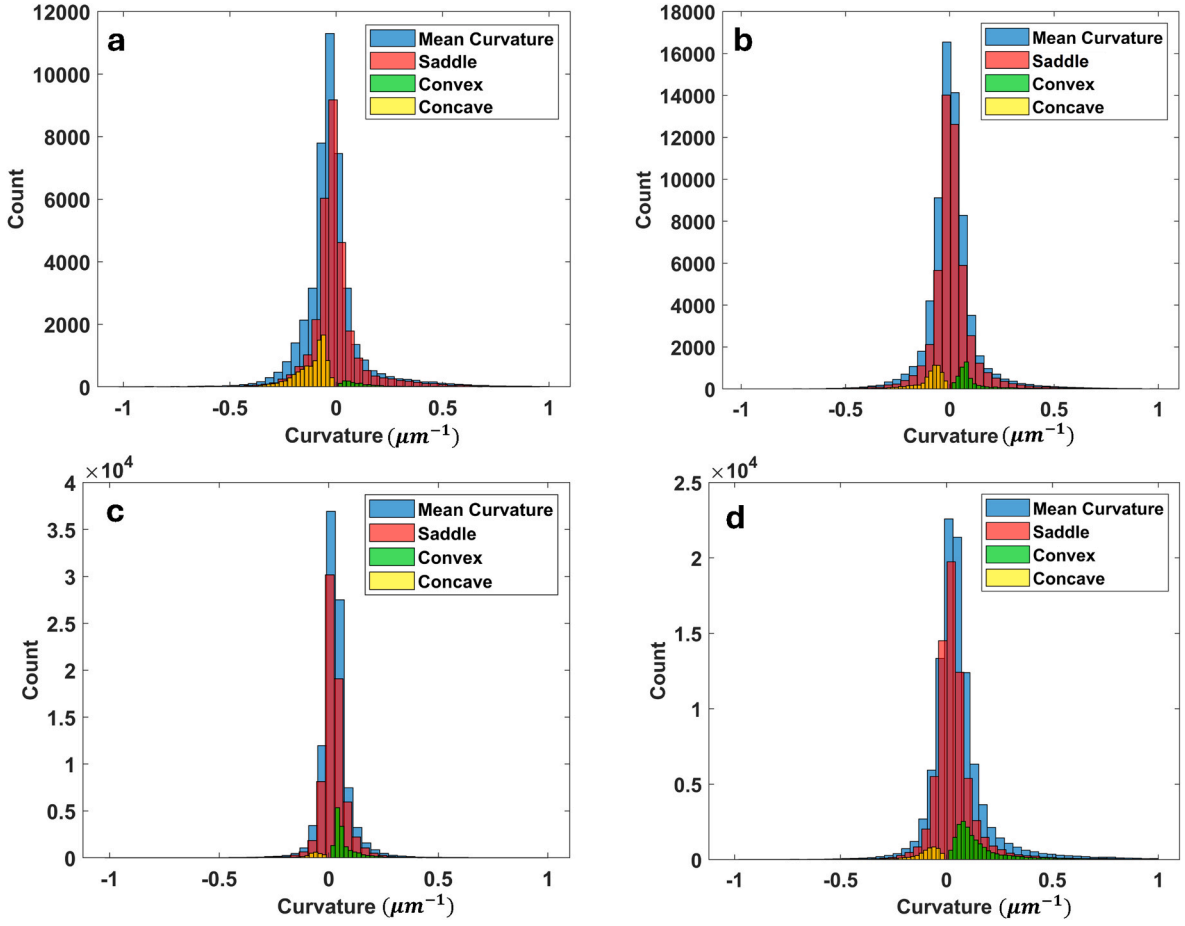

Fig. 5. (a) Curvature measurements of Uni_0.99_1 (So = 0.50); (b) curvature measurements of Uni_0.99_2 (So = 0.50); (c) curvature measurements of CB_Fixed (So = 0.50); (d) curvature measurements of experimental data (So = 0.50).

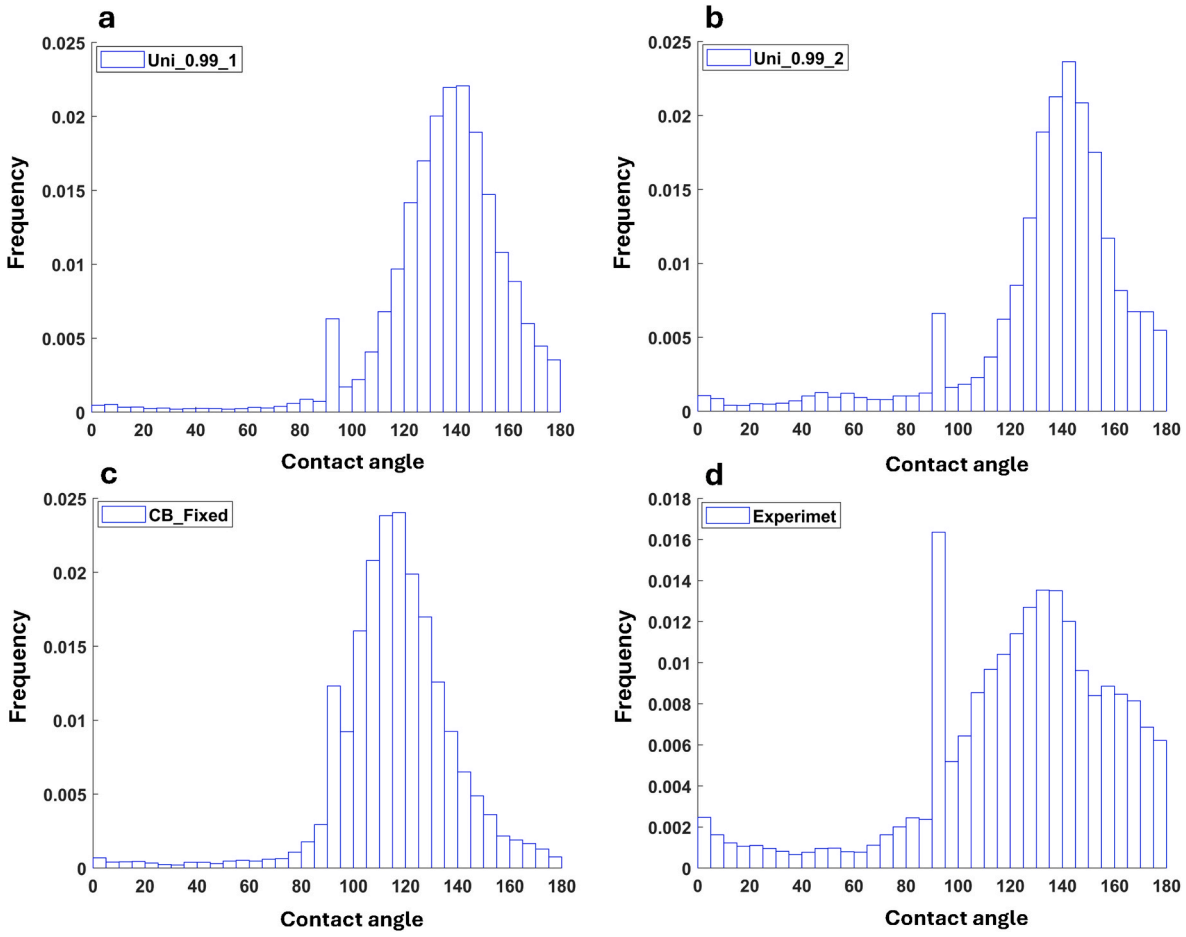

Fig. 6. (a) Contact angle measurements of Uni_0.99_1 (So = 0.50); (b) contact angle measurements of Uni_0.99_2 (So = 0.50); (c) contact angle measurements of CB Fixed (So = 0.50); (d) contact angle measurements of Experimental data (So = 0.50). The average contact angle values of them are 130°, 124°, 108° and 109°, respectively.

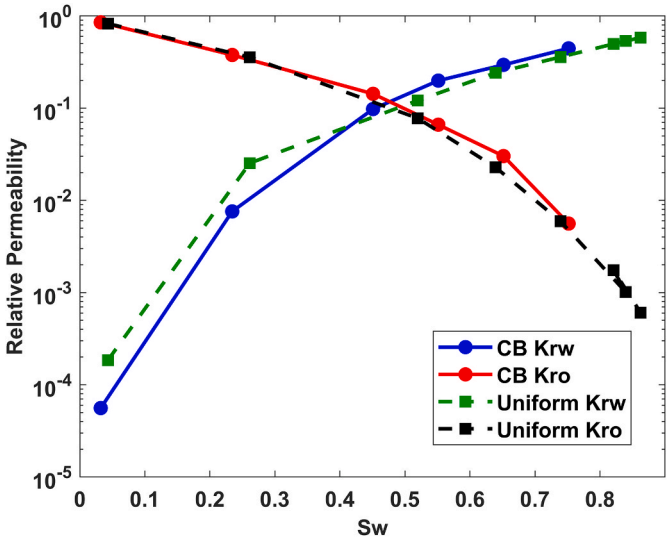

Fig. 7. Comparison of relative permeability on a logarithmic scale for Uni_0.99_2 (squares) and CB_Fixed (circles) as a function of water saturation (Sw), showing differences in residual oil saturation.

flow capacity of the non-wetting phase as compared to that in 'CB_Fixed' (Morrow, 1990; Salathiel, 1973; Sharma and Filoco, 2000).

4. Discussion

We conducted two-phase LBM simulations on Ketton limestone considering two different wetting models: (1) *Uniform Wetting* and (2) *Cassie-Baxter Wetting*. We then compared the resulting simulated morphological state of the oil to that for the mixed-wet experimental data reported in (Scanziani et al., 2020b). Based on pore-scale metrics the 'Uni_0.99_2' model provided the best approximation to the experimental data. 'Uni_0.99_2' assumed a uniform contact angle of 130° for oil-treated and 40° for untreated surfaces yet the number of water-wet macropore surface voxels in the model were negligible. Our wettability assignment was based on the initial water saturation prior to imbibition, which based on the experimental data for resolved porosity was only 0.1%. Therefore, nearly all macropore surface voxels in the 'Uni_0.99_2' model had an assigned affinity value of −0.64. Our analysis of the simulations, however, displayed minimal surfaces and a broad range of effective contact angles, which are commonly interpreted, based on experimental data, as mixed-wet conditions. From a modelling perspective, these outcomes appear to manifest from the internal displacement dynamics and/or local pore geometry rather than due to heterogeneous (or mixed-wet) surface affinity values. The degree to which minimal surfaces indicate mixed-wet conditions in experimental data has been reported by (Scanziani et al., 2020b) yet the impact of flow dynamics and pore geometry was not investigated in detail. This

could be an interesting topic for future work.

We also highlighted a difficulty with assigning surface wettability heterogeneity when working with micro-CT data. Due to the well-known partial volume effect, when applying Equation (2), surface voxels tend to have a lower solid fraction than expected, i.e., based on solid fraction measurements taken far from an interface. Therefore, the Cassie-Baxter model resulted in more water-wet oil morphologies than that observed in the experimental data. We therefore consider the spatial distribution of the microporosity (at least three voxels from an interface) to assign a similar distribution to the model domain before applying *Model 2*. As a result, the contact angle distribution from simulation provided an average value that was well aligned with that reported by (Scanziani et al., 2018). To a certain extent, this method fixed the partial volume effect, but the overall results compared to the experimental data was not as good as the results provided by the 'Uni_0.99_2' model suggesting that the overall approach of *Model 2* was not required.

Based on pore-scale morphological measures, our results suggested that a uniform wetting model best described the wetting state of the aged carbonate sample. (Akai et al., 2019) reports similar results where LBM simulations with a uniform contact angle provided accurate pore-by-pore occupancy data when compared to experimental data for an aged reservoir carbonate sample. However, (Akai et al., 2019) also reported that spatially heterogenous wettability was required to correctly predict fluid conductivity even though accurate pore-by-pore occupancy did not require spatial heterogeneity. In part, fluid conductivity is related to the morphological measures of surface area coverage and Euler characteristic given herein. However, we do not directly study fluid conductivity and instead focus on pore-scale morphologies. It should be noted that Ketton carbonate is distinctly different than the reservoir carbonate studied in (Alyafei and Blunt, 2016) and simulated in (Akai et al., 2019), which had significantly more heterogeneous pore structure and lower permeability. In comparison, Estaillades carbonate has a permeability range of 1.22–3.26 $\times$ 10^{-13} m^2, Portland carbonate ranges from 1.9 to 13 $\times$ 10^{-15} m^2, while Ketton carbonate exhibits permeability ranging from 1.07 to 3.55 $\times$ 10^{-12} m^2. In addition, the reservoir carbonate studied in [18] was aged with a macroporosity oil saturation of 99.0% while the Ketton carbonate sample was aged at 99.9% oil saturation. Differences in connate water saturation during aging are known to result in different wetting states (Rücker et al., 2020). For (Akai et al., 2019), mixed-wet conditions with a contact angle of 150° for oil-wet surfaces provided the best simulation result while herein oil-wet surfaces required a contact angle of 130°. Lastly, a commonality between our work and (Akai et al., 2019) is that an assigned advancing contact angle greater than the geometrically measured contact angle from experimental data was required for a good agreement between experiment and simulation. Our reasoning to apply a contact angle value greater than the measured value was based on observed errors in the measurement of contact angles greater than 90 ° (Sun et al., 2020). The reasoning suggested by (Akai et al., 2019) is that when a non-wetting phase displaces a wetting phase it is the largest contact angle that determines the threshold capillary pressure not the observed average value from experiments. Both points are valid and provide a general guideline for factors to consider when using geometrically measured contact angles for pore-scale simulations.

5. Conclusions

We conducted eight two-phase LBM simulations on Ketton limestone with *Model 1* and *Model 2*. Our simulation results highlight that:

- A uniform contact angle value of 130° for oil-treated surfaces was representative of the tested experimental data while the Cassie-Baxter model created a too water-wet state.
- The trends in pore-scale morphological properties observed for an aged Ketton carbonate can be captured by a uniform surface wetting condition for oil treated surfaces.
- The extension of this conclusion to other rock types and other aging conditions would require further work with the addition of bulk continuum properties for validation against experimental data.

Overall, we provide the following suggestions for the assignment of wettability to pore-scale simulations:

- Simpler wetting models can likely capture the over morphological trends during flow.
- A capillary drainage image is likely the preferred method for the generation of spatially correlated water-wet and oil-wet regions where each region is assigned a uniform value.
- Measured contact angles and interfacial curvatures from LBM simulations are a complex result of surface wetting properties, internal dynamics, and local pore geometry.
- An assigned contact angle of greater than +10° above the geometrically measured contact angle from experimental data should be used.

These suggestions are based on the specific samples studied and may vary with other samples. Future work will be required to understand the impact of fluid dynamics on the development of minimal surfaces. Also, the generation of spatially heterogeneous wetting states during the core aging procedures should be evaluated futher yet was not observed for the sample investiageted herein based on our metrics.

CRediT authorship contribution statement

Tingting Wang: Conceptualization, Data curation, Formal analysis, Investigation, Methodology, Writing – original draft. **Ying Da Wang:** Software, Writing – review & editing, Supervision. **Chenhao Sun:** Investigation, Software, Writing – review & editing. **James E. McClure:** Software, Writing – review & editing. **Peyman Mostaghimi:** Funding acquisition, Resources, Supervision, Writing – review & editing. **Ryan T. Armstrong:** Funding acquisition, Resources, Supervision, Writing – review & editing.

Declaration of competing interest

The authors declare that no financial or personal interests exist that could potentially influence the work discussed in this paper.

Data availability

Data will be made available on request.

Acknowledgements

R.T.A. and P. M. acknowledge their Australian Research Council Discovery Grant (DP210102689).

Appendix A. Minkowski Functionals

The Minkowski Functionals (MF) are geometric measures of size based on set theory (Serra, 1983), which are commonly used in porous media research (Armstrong et al., 2019). By considering the surface δX of phase (X) embedded in Euclidean space (Ω), the MFs are $d+1$ functionals, where d is the dimension of Ω. In three-dimensional (3D) space, the MF are effectively volume, surface area, integral mean curvature, and Euler characteristic. M_0

is the first functional and represents the total volume of X. M_1 is the second functional and represents the integral measure of the surface area of X, defined as

$$M_1(X) = \int_{\delta X} ds, \tag{A1}$$

where δX is the entire surface and ds is the surface element on X. M_2 is the third functional and represents the integral of mean curvature of the entire surface, which is defined as

$$M_2(X) = \int_{\delta X} \left[\frac{1}{r_1} + \frac{1}{r_2}\right] ds, \tag{A2}$$

where r_1 and r_2 are the principal radii of curvature of surface element ds. M_3 represents the integral of Gaussian curvature of the entire surface, which is defined as

$$M_3(X) = \int_{\delta X} \left[\frac{1}{r_1 \times r_2}\right] ds = 4\pi\chi(X), \tag{A3}$$

where $\chi(\delta X)$ is the Euler characteristic of the bounding surface and $\chi(X)$ is the Euler characteristic of phase X (Michielsen and De Raedt, 2001; Ohser and Mücklich, 2000). The Euler characteristic can also be described by isolated objects (N), redundant loops (L) and cavities (O), defined as

$$\chi(X) = N - L + O. \tag{A4}$$

Equation (A4) provides a more direct understanding of Euler number, i.e., a system with more loops has higher connectivity, and thus more negative Euler number.

References

Akai, T., Alhammadi, A.M., Blunt, M.J., Bijeljic, B., 2019. Modeling oil recovery in mixed-wet rocks: pore-scale comparison between experiment and simulation. Transport Porous Media 127, 393–414. https://doi.org/10.1007/s11242-018-1198-8.

Alhammadi, A.M., AlRatrout, A., Singh, K., Bijeljic, B., Blunt, M.J., 2017. In situ characterization of mixed-wettability in a reservoir rock at subsurface conditions. Sci. Rep. 7, 10753 https://doi.org/10.1038/s41598-017-10992-w.

AlRatrout, A., Blunt, M.J., Bijeljic, B., 2018. Wettability in complex porous materials, the mixed-wet state, and its relationship to surface roughness. Proc. Natl. Acad. Sci. U.S. A. 115, 8901–8906. https://doi.org/10.1073/pnas.1803734115.

AlRatrout, A., Raeini, A.Q., Bijeljic, B., Blunt, M.J., 2017. Automatic measurement of contact angle in pore-space images. Adv. Water Resour. 109, 158–169. https://doi.org/10.1016/j.advwatres.2017.07.018.

Alyafei, N., Blunt, M.J., 2016. The effect of wettability on capillary trapping in carbonates. Adv. Water Resour. 90, 36–50. https://doi.org/10.1016/j.advwatres.2016.02.001.

Anderson, W., 1986. Wettability literature survey-part 2: wettability measurement. J. Petrol. Technol. 38, 1–246.

Anderson, W.G., 1986. Wettability literature survey-part 1: rock/oil/brine interactions and the effects of core handling on wettability. J. Petrol. Technol. 38, 1125–1144.

Armstrong, R.T., McClure, J.E., Robins, V., Liu, Z., Arns, C.H., Schlüter, S., Berg, S., 2019. Porous media characterization using Minkowski functionals: theories, applications and future directions. Transport Porous Media 130, 305–335. https://doi.org/10.1007/s11242-018-1201-4.

Arnold, P., Dragovits, M., Linden, S., Hinz, C., Ott, H., 2023. Forced imbibition and uncertainty modeling using the morphological method. Adv. Water Resour. 172, 104381 https://doi.org/10.1016/j.advwatres.2023.104381.

Cassie, A.B.D., Baxter, S., 1944. Wettability of porous surfaces. Trans. Faraday Soc. 40, 546. https://doi.org/10.1039/tf9444000546.

Clausnitzer, V., Hopmans, J.W., 1999. Determination of phase-volume fractions from tomographic measurements in two-phase systems. Adv. Water Resour. 22, 577–584.

Da Wang, Y., Kearney, L., Blunt, M.J., Sun, C., Tang, K., Mostaghimi, P., Armstrong, R.T., 2024. In situ characterization of heterogeneous surface wetting in porous materials. Adv. Colloid Interface Sci., 103122

Fan, M., McClure, J.E., Armstrong, R.T., Shabaninejad, M., Dalton, L.E., Crandall, D., Chen, C., 2020. Influence of clay wettability alteration on relative permeability. Geophys. Res. Lett. 47, e2020GL088545 https://doi.org/10.1029/2020GL088545.

Fernø, M.A., Torsvik, M., Haugland, S., Graue, A., 2010. Dynamic laboratory wettability alteration. Energy Fuel. 24, 3950–3958. https://doi.org/10.1021/ef1001716.

Foroughi, S., Bijeljic, B., Lin, Q., Raeini, A.Q., Blunt, M.J., 2020. Pore-by-pore modeling, analysis, and prediction of two-phase flow in mixed-wet rocks. Phys. Rev. E 102, 023302. https://doi.org/10.1103/PhysRevE.102.023302.

Garfi, G., John, C.M., Lin, Q., Berg, S., Krevor, S., 2020. Fluid surface coverage showing the controls of rock mineralogy on the wetting state. Geophys. Res. Lett. 47 https://doi.org/10.1029/2019GL086380.

Imperial College London, Lin, Q., Bijeljic, B., , Imperial College London, Krevor, S.C., , Imperial College London, Blunt, M.J., , Imperial College London, Rücker, M., , Imperial College London, Berg, S., , Shell Global Solutions International BV, Coorn, Ab, , Shell Global Solutions International BV, Van Der Linde, H., , Shell Global Solutions International BV, Georgiadis, Apostolos, Shell Global Solutions International BV, Wilson, O.B., Shell Global Solutions International BV, 2019. A new waterflood initialization protocol with wettability alteration for pore-scale multiphase flow experiments. Petro S J. 60, 264–272. https://doi.org/10.30632/PJV60N2-2019a4.

Jackson, M.D., Valvatne, P.H., Blunt, M.J., 2003. Prediction of wettability variation and its impact on flow using pore- to reservoir-scale simulations. J. Petrol. Sci. Eng. 39, 231–246. https://doi.org/10.1016/S0920-4105(03)00065-2. Reservoir Wettability.

Jadhunandan, P., Morrow, N.R., 1995. Effect of wettability on waterflood recovery for crude-oil/brine/rock systems. SPE Reservoir Eng. 10, 40–46.

Kwok, D.Y., Neumann, A.W., 1999. Contact angle measurement and contact angle interpretation. Adv. Colloid Interface Sci. 81, 167–249. https://doi.org/10.1016/S0001-8686(98)00087-6.

Lin, Q., Al-Khulaifi, Y., Blunt, M.J., Bijeljic, B., 2016. Quantification of sub-resolution porosity in carbonate rocks by applying high-salinity contrast brine using X-ray microtomography differential imaging. Adv. Water Resour. 96, 306–322. https://doi.org/10.1016/j.advwatres.2016.08.002.

Lin, Q., Bijeljic, B., Berg, S., Pini, R., Blunt, M.J., Krevor, S., 2019. Minimal surfaces in porous media: pore-scale imaging of multiphase flow in an altered-wettability Bentheimer sandstone. Phys. Rev. E 99, 063105.

McClure, J.E., Li, Z., Berrill, M., Ramstad, T., 2021. The LBPM software package for simulating multiphase flow on digital images of porous rocks. Comput. Geosci. 25, 871–895. https://doi.org/10.1007/s10596-020-10028-9.

McPhee, C., Reed, J., Zubizarreta, I., 2015. Core Analysis: a Best Practice Guide. Elsevier.

Menke, H.P., Bijeljic, B., Andrew, M.G., Blunt, M.J., 2015. Dynamic three-dimensional pore-scale imaging of reaction in a carbonate at reservoir conditions. Environ. Sci. Technol. 49, 4407–4414. https://doi.org/10.1021/es505789f.

Michielsen, K., De Raedt, H., 2001. Integral-geometry morphological image analysis. Phys. Rep. 347, 461–538.

Morrow, N.R., 1990. Wettability and its effect on oil recovery. J. Petrol. Technol. 42, 1476–1484.

Murison, J., Semin, B., Baret, J.-C., Herminghaus, S., Schröter, M., Brinkmann, M., 2014. Wetting heterogeneities in porous media control flow dissipation. Phys. Rev. Appl. 2, 034002 https://doi.org/10.1103/PhysRevApplied.2.034002.

Ohser, J., Mücklich, F., 2000. Statistical Analysis of Microstructures in Materials Science. John Wiley & Sons.

Rücker, M., Bartels, W.-B., Singh, K., Brussee, N., Coorn, A., Van Der Linde, H.A., Bonnin, A., Ott, H., Hassanizadeh, S.M., Blunt, M.J., Mahani, H., Georgiadis, A., Berg, S., 2019. The effect of mixed wettability on pore-scale flow regimes based on a flooding experiment in Ketton limestone. Geophys. Res. Lett. 46, 3225–3234. https://doi.org/10.1029/2018GL081784.

Rücker, M., Bartels, W.-B., Garfi, G., Shams, M., Bultreys, T., Boone, M., Pieterse, S., Maitland, G.C., Krevor, S., Cnudde, V., Mahani, H., Berg, S., Georgiadis, A., Luckham, P.F., 2020. Relationship between wetting and capillary pressure in a crude oil/brine/rock system: from nano-scale to core-scale. J. Colloid Interface Sci. 562, 159–169. https://doi.org/10.1016/j.jcis.2019.11.086.

Salathiel, R.A., 1973. Oil recovery by surface film drainage in mixed-wettability rocks. J. Petrol. Technol. 25, 1216–1224.

Scanziani, A., Alhosani, A., Lin, Q., Spurin, C., Garfi, G., Blunt, M.J., Bijeljic, B., 2020a. In situ characterisation of three-phase flow in mixed-wet porous media using synchrotron imaging. https://doi.org/10.1002/essoar.10502988.1.

Scanziani, A., Lin, Q., Alhosani, A., Blunt, M., Bijeljic, B., 2020b. Dynamics of displacement in mixed-wet porous media (preprint). Engineering. https://doi.org/10.31223/OSF.IO/JPMVC.

Scanziani, A., Singh, K., Bultreys, T., Bijeljic, B., Blunt, M.J., 2018. In situ characterization of immiscible three-phase flow at the pore scale for a water-wet carbonate rock. Adv. Water Resour. 121, 446–455. https://doi.org/10.1016/j.advwatres.2018.09.010.

Serra, J., 1983. Image Analysis and Mathematical Morphology. Academic Press, Inc., USA.

Sharma, M.M., Filoco, P.R., 2000. Effect of brine salinity and crude-oil properties on oil recovery and residual saturations. SPE J. 5, 293–300.

Shojaei, M.J., Bijeljic, B., Zhang, Y., Blunt, M.J., 2022. Minimal surfaces in porous materials: X-ray image-based measurement of the contact angle and curvature in gas diffusion layers to design optimal performance of fuel cells. ACS Appl. Energy Mater. 5, 4613–4621. https://doi.org/10.1021/acsaem.2c00023.

Singh, K., Jung, M., Brinkmann, M., Seemann, R., 2019. Capillary-dominated fluid displacement in porous media. Annu. Rev. Fluid Mech. 51, 429–449. https://doi.org/10.1146/annurev-fluid-010518-040342.

Sripal, E., James, L.A., 2018. Application of an Optimization Method for the Restoration of Core Samples for SCAL Experiments 10.

Standnes, D.C., Austad, T., 2000. Wettability Alteration in Chalk 1, vol. 11. Preparation of core material and oil properties.

Sun, C., McClure, J.E., Mostaghimi, P., Herring, A.L., Meisenheimer, D.E., Wildenschild, D., Berg, S., Armstrong, R.T., 2020. Characterization of wetting using topological principles. J. Colloid Interface Sci. 578, 106–115. https://doi.org/10.1016/j.jcis.2020.05.076.

Treiber, L.E., Owens, W.W., 1972. A laboratory evaluation of the wettability of fifty oil-producing reservoirs. Soc. Petrol. Eng. J. 12, 531–540. https://doi.org/10.2118/3526-PA.

Tweheyo, M.T., Holt, T., Torsæter, O., 1999. An experimental study of the relationship between wettability and oil production characteristics. J. Petrol. Sci. Eng. 24, 179–188. https://doi.org/10.1016/S0920-4105(99)00041-8.

Wang, Y.D., Chung, T., Armstrong, R.T., McClure, J., Ramstad, T., Mostaghimi, P., 2020. Accelerated computation of relative permeability by coupled morphological and direct multiphase flow simulation. J. Comput. Phys. 401, 108966.

Wildenschild, D., Sheppard, A.P., 2013. X-ray imaging and analysis techniques for quantifying pore-scale structure and processes in subsurface porous medium systems. Adv. Water Resour. 51, 217–246. https://doi.org/10.1016/j.advwatres.2012.07.018.

Zhou, X., Morrow, N.R., 2000. Interrelationship of wettability, initial water saturation, aging time, and oil recovery by spontaneous imbibition and waterflooding. SPE J. 5, 9.